Wavelength dependence of nanosecond IR laser-induced breakdown in water: evidence for multiphoton initiation via an intermediate state

Norbert Linz[1], Sebastian Freidank[1], Xiao-Xuan Liang[1], Hannes Vogelmann[2], Thomas Trickl[2+], and Alfred Vogel[1*]

[1]*Institut für Biomedizinische Optik, Universität zu Lübeck, Peter-Monnik Weg 4, 23562 Lübeck, Germany*

[2]*Institut für Meteorologie und Klimaforschung, Forschungszentrum Karlsruhe, Kreuzeckbahnstr 19, 82467 Garmisch-Partenkirchen, Germany*

Investigation of the wavelength dependence (725 – 1025 nm) of the threshold for nanosecond optical breakdown in water revealed steps consistent with breakdown initiation by multiphoton ionization, with an initiation energy of about 6.6 eV. This value is considerably smaller than the autoionization threshold of about 9.5 eV, which can be regarded as band gap relevant for avalanche ionization. Breakdown initiation is likely to occur via excitation of a valence band electron into a solvated state, followed by rapid excitation into the conduction band. Theoretical analysis based on these assumptions suggests that the seed electron density required for initiating avalanche ionization drops from 2.5×10^{15}cm^{-3} at 725 nm to 1.1×10^{12}cm^{-3} at 1025 nm. These results demand changes of future breakdown modeling for water including the use of a larger band gap than previously employed, the introduction of an intermediate energy level for initiation, and consideration of the wavelength dependence of seed electron density.

PACS numbers: 79.20.Ds, 79.20.Ws, 42.62.Fi, 42.62.Be

79.20.Ds Laser beam impact phenomena
79.20.Ws Multiphoton absorption
42.62.Fi Laser spectroscopy
42.62.Be Biological and medical laser applications

1. INTRODUCTION

IR laser-induced breakdown in water and aqueous media is utilized for microsurgery in transparent tissues [1-3] and cells [4-6] as well as for producing spherical bubbles in basic investigations of cavitation bubble dynamics [7]. Theoretical modeling of the breakdown process requires a clear picture on the fundamental mechanisms providing seed electrons for avalanche ionization, as well as a profound knowledge of the band structure of liquid water and the possible excitation pathways between valence band (VB) and conduction band (CB). In this study, both issues are addressed by investigating the wavelength dependence of the breakdown threshold in water for nanosecond (ns) IR laser pulses.

Avalanche ionization (AI) is the most powerful mechanism driving IR ns laser-induced dielectric breakdown. It depends on the availability of seed electrons in the CB that can gain energy through inverse bremsstrahlung absorption (IBA) and multiply by impact ionization. For ns breakdown, it is still a matter of debate whether such seed electrons are available as background electrons [8,9], formed at impurities [10-12], or whether they are generated by multiphoton ionization (MPI) of the water itself [4,13,14]. It is generally acknowledged that femtosecond (fs) and picosecond (ps) IR breakdown is initiated by photoionization because ultrashort pulses are sufficiently powerful for supporting higher order multiphoton processes [15-18]. However, conclusive evidence for the relevance of photoionization in ns breakdown is still lacking. If breakdown initiation depends on MPI, the wavelength dependence of the breakdown threshold, $I_{th}(\lambda)$, should exhibit a sharp rise whenever one photon more is needed to overcome the initiation energy E_{ini} [19]. By contrast, if it relies on background electrons or thermal ionization of impurities, the $I_{th}(\lambda)$ curve should vary monotonously.

In this paper, we investigate the optical breakdown threshold in water at 21 wavelengths between 725 nm and 1025 nm in order to probe the existence of steps in the $I_{th}(\lambda)$ spectrum verifying multiphoton-initiation of nanosecond IR breakdown. Evaluation of the distance between such steps could then provide information on the initiation energy E_{ini} that is required to start AI.

Previously, E_{ini} has been identified with the band gap of water, E_{gap}. In 1991, Sacchi introduced a breakdown model based on Williams' concept of treating water as an "amorphous semiconductor" [20], in which Sacchi assumed that valence band and conduction band are separated by an energy gap of 6.5 eV [11,21]. Since then, this approach has been adopted by numerous researchers designing models for optical breakdown in water. Most

researchers followed Sacchi in using a band gap of 6.5 eV [4,13,14,22-27], while in some recent studies values of 7 eV [28] and 8 eV [29] were employed. However, spectroscopic evidence collected in the past two decades suggests that Sacchi's approach oversimplifies the band structure of water. Effective direct ionization into the conduction band was found to occur only at considerably higher excitation energies ≥ 9.5 eV [30,31], and what was previously considered as "ionization energy" of 6.5 eV is actually the minimum energy needed for direct excitation of a VB electron into a solvated state [32]. It was shown in the 1990's that the creation of solvated electrons does not require an intermediate excitation into the CB followed by subsequent "dissolution," as had been previously assumed [33] but can also occur directly [34,35]. This implies that the actual band gap is larger than 6.5 eV, and that breakdown initiation may occur as a two-step process involving the generation of solvated electrons, e_{aq}^-, and their subsequent upconversion into the CB. Literature data supporting this corollary are presented in Figs. 1(a) - (d) and interpreted in Figs. 1(e) and 2.

The data of Fig. 1 and the excitation/ionization pathways presented in Fig. 2 will now be discussed step-by-step to substantiate the possibility of breakdown initiation via solvated electron generation and to identify an appropriate value for the band gap of water. The first step in creating e_{aq}^- involves promotion of valance band electrons into the $\tilde{A}\ 1^1B_1$ absorption band, which reaches down to about 6 eV [20,36]. Formation of e_{aq}^- at energies far below the CB requires the existence of pre-existing trap sites consisting of favorable local arrangements of water molecules that can accommodate the electron [32,37,38]. An ideal trap corresponds to a constellation of six water molecules with their OH bonds directed towards the electron [37-39]. When an excited water molecule is located close to such a trap, an excess electron can be abstracted and hydrate within less than 300 fs [38,40]. This process involves rapid proton transfer to a neighboring water molecule resulting in the formation of a OH_{aq} radical and a hydronium ion $H_3O_{aq}^+$ [35,41-43]. Its onset corresponds to the threshold energy for solvated electron formation, $E_{\text{thsolv}} \approx 6.4$ eV [20,32,36,44] [Fig. 1(a)]. Solvated electron formation at such low energies has been explained by the red-shift of the vapor $\tilde{A}\ 1^1B_1$ absorption band compared to that of liquid water [32,45]. Water molecules located near void-like trap sites will be able to absorb photons of lower energies and, at the same time, provide a favorable environment for electron solvation [32,46].

Part of the solvated electrons, e_{aq}^-, will undergo geminate recombination with their hydronium counter-ion within a 1-200 ps time scale [35], while the escaping fraction has a much longer life time of ≈ 300 ns [44]. Data for the energy dependence of escape quantum efficiency QE_{esc} from Ref. [32] are given in Fig. 1(a). The geminate recombination kinetics can be traced by time-resolved measurements of e_{aq}^- absorption [30,35,47]. Comparison of absorption values at early and late times provides the escape probability P_{esc} in Fig. 1(b). The initial quantum efficiency is then obtained as $QE_{ini} = QE_{esc} / P_{esc}$ [Fig. 1(d)].

For low excitation energy, E_{exc}, the average distance between a solvated electron and its source, the "ejection length" r_{ej}, is only 1.1 nm [30] [Fig. 1(c)]. With increasing excitation energy E_{exc}, electrons can be accommodated also by initially less perfect configurations of water molecules, since part of E_{exc} is now available for rearranging the molecules in the process of electron abstraction. For 7.8 eV < E_{exc} < 9.5 eV, the trap density, χ_{trap}, increases exponentially, the traps become shallower, and more e_{aq}^- can be produced [32] [Fig. 1(a)]. However, in this energy range, the increase of E_{exc} mainly allows for an occupation of more traps but does not yet significantly increase the average e_{aq}^- ejection length [Fig. 1(c)].

For E_{exc} ≥ 9.5 eV, both ejection length and escape probability of the electrons increase significantly [Figs. 1(b) and (c)]. This indicates that excitation into the CB becomes possible in an "autoionization" process, which involves reorganization of the excited water molecule into a form with lower ionization potential [30,31,41,45,48]. Above the threshold for vertical ionization, where nuclear position remain unchanged, the electron ejection length finally reaches a value of about 4 nm [30,49] [Fig. 1(c)]. The vertical excitation energy into the CB in liquid water is ≈ 11 eV [30,45,50], slightly lower than the excitation energy into vacuum from bulk liquid water [51]. However, since the threshold for autoionization is lower (at around 9.3 eV) and because its probability increases strongly for E_{exc} ≥ 9.5 eV, an energy level 9.5 eV above the valence band is regarded as lower edge of the conduction band [30].

The possibility of breakdown initiation via e_{aq}^- formation depends critically on the density of pre-existing traps, χ_{trap}. An estimate of χ_{trap} can be obtained by relating the initial quantum efficiency for solvated electron formation to the ejection radius of the excess electrons, r_{ej}: $\chi_{trap} = QE_{ini} / (4/3\pi r^3_{ej})$. The result is shown in Fig. 1(e). For determining χ_{trap} near the threshold of solvated electron formation, we used the measured QE_{ini} value for 6.42 eV, and an r_{ej} value (1.04 nm) that was estimated by extrapolation from the 7.8 eV - 9.3 eV

energy range, where r_{ej} is almost constant. This yields $\chi_{trap} = 0.73\times10^{19}\text{cm}^{-3}$, in agreement with a theoretical estimate in Ref. [52]. Between 6.4 eV and 7.8 eV excitation energy, χ_{trap} remains in the order of 10^{19}cm^{-3} and increases rapidly thereafter.

The large trap density even at small excitation energies suggests the possibility of breakdown initiation via e^-_{aq} generation followed by upconversion into the CB as depicted in Fig. 2. Upconversion is facilitated by the long lifetime of solvated electrons that have escaped geminate recombination, which is ≈ 300 ns [44]. In IR breakdown, it can occur either via multiphoton absorption, or via stepwise excitation through intermediate *p*-states [53]. Both ground state and *p* states absorb well in a broad wavelength range from below 500 nm to above 1100 nm [33,38,44,54,55].

In this study, the hypothesis on multiphothon-initiation of optical breakdown via an intermediate energy level between valance and conduction band is experimentally explored through breakdown threshold spectroscopy. Measurements are performed using single-longitudinal mode (slm) laser pulses providing a smooth, reproducible temporal pulse shape that is essential for a precise threshold determination [19,56,57]. The $I_{th}(\lambda)$ spectrum exhibits peaks consistent with an initiation energy E_{ini} = 6.6 eV, slightly above the threshold for solvated electron formation. A simple theoretical analysis of the measurement results further corroborates our hypothesis on breakdown initiation, and provides an estimate of the wavelength-dependent seed electron density needed to initiate avalanche ionization.

2. EXPERIMENTAL METHODS

The experimental setup for optical breakdown threshold spectroscopy is depicted in Fig. 3. Infrared (IR) ns laser pulses are focused at high numerical aperture (*NA*) through long-distance water-immersion objectives (Leica HCX APO L U-V-I, 63×/*NA* = 0.9 and 40×/*NA* = 0.8) into deionized and filtered (0.2 µm) water. The objectives are inserted into the wall of the water cell to guarantee aberration-free focusing of the laser pulses. The rear entrance pupil of each objective was slightly overfilled to create a uniform irradiance distribution corresponding to an Airy pattern in the focal plane. Breakdown is identified with the occurrence of bubble formation that is detected using the scattering of a continuous probe laser beam adjusted collinear and confocal with the pulsed laser beam. The maximum bubble radius R_{max} is deduced from the lifetime of the first oscillation cycle of the cavitation bubble, T_{osc}, which can readily be obtained from the scattering signal [58].

Laser pulses with smooth temporal shape and tunable wavelength (725-1025 nm) were generated by a single-frequency optical parametric oscillator (OPO; Continuum model Mirage with oscillator only), pumped by the second-harmonic output from an slm Nd:YAG laser (Continuum, Powerlite 8020). A special resonator configuration of the OPO is required to achieve slm pulses; pumping of regular OPOs with a slm pump laser alone does not yet avoid the spiking arising from statistical interference of longitudinal resonator modes. The OPO is a modified version [59] of the commercial instrument, which is based on a short (≈ 5 cm) Littmann cavity and a KTP crystal for parametric frequency conversion [60]. In the modified version, the vertical diameter of the 532-nm pump beam is compressed by a factor of two with a cylindrical telescope to suppress out-of-plane modes in the OPO emission, which results in a lower frequency jitter and a greatly improved slm performance. The wavelength is actively stabilized to within ± 35 MHz by piezo-electrically adjusting the tilt angle of the tuning mirror according to the output of an interferometric wave meter (Cluster, LM007). Depending on wavelength, the OPO emits pulses of 1.5 - 3.0 ns duration and 0.1 - 0.5 mJ energy at 20 Hz repetition rate, with < 0.4 mrad beam divergence. The single-shot bandwidth of 2.0-ns-pulses is 250 MHz, which is almost Fourier-transform limited.

Shape and duration of each laser pulse employed for the threshold determination are measured using a fast photodiode (ANTEL AR-S1) with 100 ps rise time and a digital oscilloscope with 6 GHz analog bandwidth (Tektronix DPO 70604). A Gaussian function was fitted to the experimental data to obtain the exact value of the FWHM time. Figure 4(a) shows the shape of a typical pulse emitted by the slm OPO. For reference, Figs. 4(b) and (c) show a comparison with single-frequency and multimode Nd:YAG laser pulses.

To determine M^2, we used a Hartman Shack wavefront analyzer manufactured by Laser-Laboratorium Göttingen e.V., Germany that provides all beam parameters in a single shot measurement. As the beam is not circular symmetric, values in the transverse x and y directions are determined, and the average value is obtained as $M^2 = \sqrt{M_x^2 M_y^2}$. The M^2 values and durations of all laser pulses used in the present study are presented in Fig. 5.

The pulse energy is adjusted by rotating a Fresnel-rhomb retarder in front of a Glan laser prism. The energy in front of the microscope objectives was calibrated by a reference measurement for each wavelength, and the wavelength dependence of the transmittance of the objectives is considered using data provided by the manufacturer.

Breakdown energy thresholds (E_{th}) were determined by counting how frequently bubble formation occurred as the energy was increased from sub-threshold to super-threshold values. Data were binned into small energy intervals ($n \geq 15$) with > 20 events per interval, and fitted using the Gaussian error function. E_{th} corresponds to 50 % breakdown probability. The bubble radius R_{max} at threshold was $\approx 80\,\mu m$ for $NA = 0.9$, and $\approx 100\,\mu m$ for $NA = 0.8$ for all OPO wavelengths. This provides a clear threshold criterion, since the measurement technique enables us to detect bubbles down to $R_{max} \approx 0.15\,\mu m$ [58].

Measurements corresponding to the different laser pulse shapes of Figs. 4(a) - (c) are presented in Figs. 4(d) - (f). The threshold sharpness is given by $S = E_{th} / \Delta E$, with ΔE being the energy range between 10 % and 90 % breakdown probability. For the OPO, it amounts to $S = 8.8$ [Fig. 4(d)], somewhat lower than the value of S = 25 for a slm single-wavelength Nd:YAG laser pulse [Fig. 4(e)] but considerably higher than the threshold sharpness for a multimode laser pulse that amounts to S = 2.7 [Fig. 4(f)]. Threshold sharpness is correlated to the smoothness of the temporal laser pulse shape that, in turn, depends on the slm performance of the respective laser system. The high threshold sharpness achieved with slm OPO pulses enables a precise recording of the $I_{th}(\lambda)$ spectrum.

The threshold irradiance I_{th} was calculated using the equation

$$I_{th} = \frac{E_{th}}{\tau_L \, \pi \, (M^2 d / 2)^2} \times 3.73. \qquad (1)$$

Here τ_L denotes the laser pulse duration, M^2 is the beam quality parameter, and d is the diffraction-limited diameter of the Airy pattern arising from focusing a beam with top-hat profile of wavelength λ, which is given by $d = 1.22\lambda/NA$. The factor 3.73 relates the average irradiance values within the pulse duration and focal spot diameter to the respective peak values, which determine the onset of optical breakdown phenomena.

3. WAVELENGTH DEPENDENCE OF THE BREAKDOWN THRESHOLD

The experimentally determined wavelength dependence of the breakdown threshold for focusing at $NA = 0.8$ and $NA = 0.9$ is presented in Fig. 6, together with the averaged values from both data sets. The $I_{th}(\lambda)$ spectrum exhibits two pronounced steps with peaks at 738 nm and 965 nm, each followed by a gradual decay with increasing wavelength. The steps suggest that multiphoton absorption is responsible for breakdown initiation because in that case I_{th}

should increase at those wavelengths for which an additional photon is required to provide the excitation energy for seed electron generation [19]. If initiation relied on the existence of background electrons or on thermal ionization of particulate impurities, the $I_{th}(\lambda)$ curve should vary monotonously. If it were based on multiphoton ionization of impurities providing centers of reduced excitation energy within the band gap of water, such centers should possess various different energy levels. Therefore, one would not expect to detect sharp peaks of the $I_{th}(\lambda)$ curve at few specific wavelengths. The existence of pronounced peaks with a sharp rise at their lower-wavelength side is indicative for one intrinsic energy level in liquid water, consistent with our hypothesis that breakdown initiation proceeds via e^-_{aq} generation followed by upconversion into the CB.

In the entire wavelength range between 725 nm and 1025 nm, the laser-produced bubbles had a radius ≥ 80 μm already at threshold, much larger than the sub-micrometer bubbles produced at the threshold of IR fs breakdown [58]. The vigorous character of IR ns breakdown is due to the high irradiance needed for producing seed electrons by multiphoton ionization. Once started, the ionization avalanche proceeds rapidly to full ionization [4].

A key role of multiphoton ionization is suggested also by the correlation of threshold sharpness with the pulse shape of nanosecond laser pulses, which is seen in Fig. 4 and was reported also in Refs. [56,57]. The threshold behavior is stochastic for "regular" Nd:YAG laser pulses exhibiting picosecond intensity spiking from longitudinal mode beating that changes from pulse to pulse but is highly reproducible when temporally smooth slm laser pulses are used. The correlation of stochastic behavior with the occurrence of fluctuating intensity peaks in the laser pulse implies the involvement of intensity-dependent nonlinear effects such as multiphoton processes in the breakdown initiation. By contrast, generation of seed electrons by thermal ionization from impurities would rely on deposited energy rather than on peak intensity, i.e. pulses with different shapes as in Figs. 4(b) and (c) would have the same seed electron yield and thus threshold behavior as long as their energy is the same.

The separation of the peaks in the $I_{th}(\lambda)$ curve in Fig. 6 provides information about the energy E_{ini} needed for multiphoton initiation of breakdown. The peaks at 738 nm and 965 nm and the minima at 730 nm and 947 nm, respectively, reflect a stepwise transition from an k-photon process to an (k+2)-photon process within the investigated wavelength range. E_{ini} values corresponding to different k values ranging from k = 3 to k = 5 were determined by evaluating the location of both the peaks and the minima in the $I_{th}(\lambda)$ spectrum. A transition

from a 3-photon to a 5-photon process would match with E_{ini} = 5.14 ± 0.07 eV. This excitation energy corresponds to a wavelength of 241 nm for which water is highly transparent [61], and lies well below the threshold for solvated electron generation of about 6.4 eV (Fig. 1a). The transition from a 4-photon to a 6-photon process corresponds to E_{ini} = 6.64 ±0.14 eV, which is slightly above E_{thsolv}. Finally, the transition from a 5-photon to a 7-photon process matches with E_{ini} = 8.13 ±0.34 eV, far above the threshold energy for e^-_{aq} creation. Thus, the wavelength separation of the peaks is consistent with $E_{ini} \approx 6.6$ eV. This result supports our hypothesis on stepwise initiation of IR ns breakdown consisting of multiphoton-exitation of valence band electrons into pre-existing trap sites followed by upconversion of e^-_{aq} into the conduction band.

Why is the value E_{ini} = 6.6 eV for breakdown initiation slightly higher than E_{thsolv}? Creation of the critical seed electron density ρ_{seed} needed to initiate avalanche ionization requires a critical density of solvated electrons that, in turn, depends on the number density of pre-existing trap sites. At threshold, perfect configuration of all water molecules constituting the trap is required. With increasing E_{exc}, electrons can be accommodated also by initially less perfect configurations, since part of E_{exc} is now available for rearranging the molecules in the process of electron abstraction. As a consequence, both trap density and solvated electron yield increase with increasing E_{exc} (Fig. 1). The measured value of E_{ini} represents the minimum excitation energy at which the critical seed electron density ρ_{seed} can be produced.

Zones with a distinct order of multiphoton process are separated by transition zones (indicated as grey bars in Fig. 6). In these transition zones, an MPI process of order k that just exceeds E_{ini} probably mixes with a process of order (k+1) that possesses a lower probability but can address states with higher density. The contribution of the lower-order process diminishes with increasing wavelength because E_{ini} is surpassed by an ever smaller amount, and the (k+1) process must take over when the lower-order process does not reach E_{ini} anymore. The wavelengths at which this occurs demarcate the peaks of the $I_{th}(\lambda)$ spectrum.

Both peaks of the $I_{th}(\lambda)$ curve are followed by a gradual decay with increasing wavelength, and the peak in the $I_{th}(\lambda)$ curve at 965 nm is lower than the peak at 738 nm. The overall decrease of threshold irradiance with increasing wavelength is puzzling at first sight because MPI initiation becomes harder for higher orders of the multiphoton process. However, it can be explained by considering the spatio-temporal dynamics of the onset of IR ns breakdown. For breakdown to occur, ‘local’ avalanches arising from individual seed

electrons must merge into a 'global' avalanche encompassing the focal volume. Since the seed electron density produced by the high-order multiphoton process is relatively small, the range of the local avalanches becomes relevant for breakdown initiation. This range is wavelength-dependent because the avalanche ionization rate increases approximately proportional to λ^2 as shown in Fig. 7. Calculations were performed using Kennedy's formulation of the Drude-Shen model [13,14]. Due to the increase of the AI rate with λ, 'local' avalanches arising from individual seed electrons will reach farther at longer wavelengths. Therefore, breakdown becomes possible with smaller ρ_{seed} and, hence, at lower irradiance.

The decay of the $I_{\text{th}}(\lambda)$ curve between the peaks is partially due the wavelength dependence of ρ_{seed}, and partially caused by the weak increase of the multi-photon ionization rate with increasing λ in each wavelength range spanned by the same order k of the multiphoton process that is seen in Fig. 7. The wavelength dependence of MPI was calculated using the respective approximation of the Keldysh theory [13,14,62] (see Eq. (3) further below).

The estimated trap density at 6.6 eV excitation energy, $\chi_{\text{trap}} \approx 10^{19}$ cm^{-3}, allows for a large seed electron density. However, the critical value for the initiation of IR ns breakdown will be much lower because ionization avalanches emerging from individual seed electrons spread rapidly by electron diffusion enlarging the active volume for inverse bremsstrahlung absorption, which in turn enlarges the source for further diffusion. During a ns laser pulse, local avalanches can, thus, extend much farther than the ejection length of an electron upon its promotion into the conduction band (about 4 nm). If local avalanches reach 10-100 times farther, seed electron densities between 10^{15} cm^{-3} and 10^{12} cm^{-3} will suffice to produce homogeneous plasma. More precise values of ρ_{seed} will be obtained by comparing the experimental $I_{th}(\lambda)$ spectrum to the predictions of a simple model of breakdown initiation.

4. MODELING OF BREAKDOWN INITIATION FOR IR NS PULSES

For IR ns breakdown, the creation of seed electrons by multiphoton ionization is the critical hurdle for the occurrence of breakdown. This makes it possible to establish a simple model for breakdown initiation. We assume that the generation of excited water molecules preceding the formation of solvated electrons determines I_{th} because a high-order multiphoton process is needed to provide E_{ini}. Subsequent excitation into the CB likely can follow immediately

because the energy gap is smaller (3 eV), contains intermediate energy levels, and both solvated electrons and their excited *p* states have a large absorption cross section even for low-energy photons [38,53,54]. As the photon flux during optical breakdown is very high, any electron that has overcome the first hurdle of high-order multiphoton excitation across the energy gap E_{ini} will readily be promoted into the CB [63]. To facilitate modeling, we neglect the details of the excited state absorption and assume that all excess electrons escaping geminate recombination are elevated into the CB.

Under these assumptions, the rate of stepwise CB electron generation via the "initiation channel" can be described by:

$$\frac{d\rho_{ini}}{dt} = \eta_{MPE}(E_{ini}) - \frac{\rho_{ini}}{\tau_{gem-rec}} \tag{2}$$

Here η_{MPE} denotes the rate of multiphoton excitation resulting in e^-_{aq} formation that is formulated in analogy to Keldysh's expression for pure multiphoton ionization [13,14,62]:

$$\eta_{MPE} = \frac{2\omega}{9\pi}\left(\frac{m\omega}{\hbar}\right)^{3/2} \times \exp\left(2k \times (1 - \frac{1}{4\gamma^2})\right) \times \Phi\left[\left(\sqrt{2k - \frac{2\tilde{\Delta}}{\hbar\omega}}\right)\right] \times \left(\frac{e}{16 m E_{ini} \omega^2 c \varepsilon_0 n_0}\right)^k \times I^k . \tag{3}$$

The term $\Phi[\ ]$ denotes the Dawson integral. The Keldysh parameter γ, the effective excitation potential $\tilde{\Delta}$ for ionization via the initiation channel, and the order *k* of the multiphoton process are given by:

$$\gamma = \frac{\omega}{e}\sqrt{\frac{c\,\varepsilon_0\, n_0\, m\, E_{ini}}{I}}, \tag{4}$$

$$\tilde{\Delta} = E_{ini}\left(1 + \frac{1}{4\gamma^2}\right), \tag{5}$$

and

$$k = \left\langle \frac{2\pi\tilde{\Delta}}{h\omega} + 1 \right\rangle, \tag{6}$$

where ω denotes the optical frequency, *e* the electron charge, *c* the vacuum speed of light, ε_0 the vacuum dielectric permittivity, n_0 the index of refraction of the medium, *h* Planck's constant, and *m* the exciton reduced mass. It is given by the effective masses m_e of e^-_{aq} and m_h of its counterion through $1/m = 1/m_e + 1/m_h$. We assume $m \approx m_e/2$. For nanosecond breakdown, $\gamma >> 1$, and the excitation potential $\tilde{\Delta}$ can be approximated by E_{ini}. The time

constant $\tau_{gem\text{-}rec}$ for geminate recombination in Eq. (2) was experimentally found to be about 60 ps [35,47].

Equation (2) describes the evolution of CB electron density produced via the initiation channel. Breakdown will occur, once ρ_{ini} exceeds ρ_{seed}. Eq. (2) was solved numerically for Gaussian laser pulses of 2 ns duration (FWHM) using an adaptive Runge-Kutta method [4]. The breakdown threshold was determined by iterative variation of peak irradiance until the target value of ρ_{seed} was reached.

Figure 8 presents fits of calculated breakdown threshold spectra to the measured $I_{th}(\lambda)$ curves (average values from both *NA*s). In a first step, ρ_{seed} was assumed to be constant over the wavelength range covered by our investigations, and a value of $\rho_{seed} = 3.3\times10^{14}$ cm^{-3} was obtained as best fit for $E_{ini} = 6.6$ eV [Fig. 8(a)]. However, the experimentally observed overall decrease of I_{th} with increasing wavelength could be reproduced only with a wavelength-dependent ρ_{seed} reflecting the increasing speed of avalanche ionization for longer wavelengths. Good agreement was obtained using the fitting law $\rho_{seed}(cm^{-3}) = 10^{A\lambda(nm)+B}$, with A = -0.014 nm^{-1}, and B = 26.0. With constant E_{ini} = 6.6 eV, the distance between the peaks in the predicted $I_{th}(\lambda)$ spectrum is slightly smaller than in the experimental curve. A better agreement with the experimental $I_{th}(\lambda)$ spectrum could be achieved by assuming a weak wavelength dependence of E_{ini} that reflects the wavelength dependence of ρ_{seed}. A linear decrease from $E_{ini} = 6.7$ eV at the position of the first peak (738 nm) to $E_{ini} = 6.43$ eV at the position of the second peak (965 nm) leads to the fit in Fig. 8(b). Fitting parameters for $\rho_{seed}(\lambda)$are A = -0.012 nm^{-1}, and B = 23.5. This fit represents a drop of ρ_{seed} from 2.5×10^{15}cm^{-3} at 725 nm to 1.1×10^{12}cm^{-3} at 1025 nm.

Thus, the comparison of model predictions to the measured $I_{th}(\lambda)$ spectrum suggests a pronounced wavelength dependence of ρ_{seed} and a weak $E_{ini}(\lambda)$ dependence. Both reflect the increasing rate of avalanche ionization for longer wavelengths. From 725 nm to 1025 nm, ρ_{seed} drops by three orders of magnitude, and for $\lambda \geq 1000$ nm and large NAs, single seed electrons will suffice to initiate breakdown. In this regime, E_{ini} is predicted to be close to the threshold for solvated electron generation of ≈ 6.4 eV.

The calculated $I_{th}(\lambda)$ spectrum in Fig. 8(b) exhibits sharp steps at wavelengths, where the order of the multiphoton process increases, whereas the experimental curve features well-resolved transition zones. As already discussed in section 3, these zones can be explained by

assuming that a multiphoton process of order k, which just exceeds E_{ini}, mixes with a process of order (k+1) that possesses a lower probability but can address states with higher density. The relative importance of the higher order process grows with increasing wavelength, until it takes over when the lower-order process does not reach E_{ini} anymore. The simple initiation model predicts sharp steps at the $k\rightarrow$ (k+1) transitions because it does not consider the excitation-energy dependence of trap density.

Fig. 9 presents the temporal evolution of electrons entering the CB via photoionization for λ = 800 nm. The overwhelming majority of seed electrons originate from the initiation channel described by Eq. (2). It is known from previous work that the electron density in IR ns breakdown rapidly increases to full ionization when avalanche ionization sets in [4]. The rapid increase after the critical seed electron density for avalanche ionization is reached (45 ps after the peak of the laser pulse) is indicated by an arrow. The breakdown dynamics depicted in Fig. 9 reflects the fact that for IR nanosecond breakdown the irradiance threshold for ρ_{seed} generation coincides with the breakdown threshold I_{th}. The situation differs for shorter pulse durations and wavelengths at which seed electrons produced by photoionization are readily available. Here, both photo- and avalanche ionization rate affect the rate of free-electron generation during the entire breakdown process, and the whole breakdown dynamics must be considered to determine I_{th} [4,64].

The results obtained for the initiation of IR ns breakdown in water will largely apply also to plasma formation in transparent cells and tissues. However, in those media bio-molecules can provide additional sources for free-electron generation, and the breakdown threshold may be lowered if the respective excitation energies in these alternative initiation channels are lower than E_{thsolv} for water.

5. CONCLUSIONS FOR BREAKDOWN MODELING IN GENERAL

Together with recent spectroscopic findings the present results obtained by optical breakdown threshold spectroscopy can be used to update the basic assumptions for breakdown modeling of water. Spectroscopic literature suggests that a band gap energy E_{gap} = 9.5 eV seems appropriate to consider both vertical and autoionization into the CB. The present investigations on IR ns breakdown revealed two pronounced peaks in the $I_{th}(\lambda)$ spectrum between 725 nm and 1025 nm. The existence of these peaks provides evidence that breakdown initiation relies on multiphoton ionization. Their separation correlates with an excitation energy of, on average, 6.6 eV that is slightly above the threshold for e^-_{aq}

generation. We conclude that breakdown initiation proceeds via excitation of valence band electrons into the $\tilde{A}\ 1^1B_1$ absorption band, followed by their hydration and subsequent upconversion of e^-_{aq} into the conduction band starting at 9.5 eV.

The need for correcting the band structure of water became apparent already in several recent studies in which no satisfactory agreement of model predictions with experimental results could be achieved when a band gap of 6.5 eV was used. For modeling femtosecond breakdown at 800 nm wavelength, researchers had to assume a larger band gap of 8 eV [29], or a slightly larger band gap of 7 eV in conjunction with a relatively long collision time of 10 fs [28] to match predicted and measured I_{th} values. Other researchers continued to use E_{gap} = 6.5 eV but adjusted the cross section for multiphoton ionization [24]. The present study provided evidence that not only the band gap value must be adjusted but also an intermediate energy level must be introduced into breakdown models for water. When the spectroscopically supported value of $E_{gap} \approx 9.5$ eV is employed without an intermediate energy level, the predicted breakdown threshold is much larger than for a band gap of 6.5 eV. For $E_{gap} = 9.5$ eV, $\lambda =$ 800 nm, $\tau_L = 2$ ns and $\rho_{seed} = 3.7\times10^{15}$cm^{-3}, the predicted value amounts to 2.6×10^{12} W/cm^2, which is 6 times larger than the experimental result. Therefore, the correct bandgap value of 9.5 eV can be used only in conjunction with an additional initiation channel considering the excitation path via the intermediate solvated state level of $E_{ini} = 6.6$ eV.

For IR ns pulses, use of the corrected band gap of 9.5 eV together with the introduction of a separate initiation channel with $E_{ini} \approx 6.6$ eV will lead to little changes of threshold predictions as compared to previous breakdown models. Since multiphoton initiation is the critical hurdle for the occurrence of IR ns breakdown, and E_{ini} is very close to the previously assumed band gap value of 6.5 eV [4,11,13,14,21-27], the breakdown threshold will remain almost the same. The larger band gap value will affect mainly the electron and energy density reached at the end of the breakdown process, which are determined by the avalanche ionization rate that is lower for a larger band gap. The situation differs for shorter pulse durations and wavelengths at which seed electrons produced by photoionization are readily available. Here, the lower avalanche ionization rate associated with $E_{gap} = 9.5$ eV affects the entire breakdown process. Therefore, both the breakdown threshold and the energy density at the end of the pulse are influenced by the correction of the band gap value, even with an intermediate level at 6.6 eV [64].

The possible width of the initiation channel is determined by the density of traps that can accommodate solvated electrons. In "native" liquid water at room temperature, the trap density is in the order of 10^{19} cm^{-3}, which is 4-7 orders of magnitude higher than the critical seed electron density required for AI initiation in IR ns breakdown. Thus, breakdown initiation is certainly possible, and the few seed electrons in the CB will not act back on the initiation channel. However, the trap density will probably be influenced by the subsequent breakdown process. While the band gap itself is fairly stable because it relies on the $\tilde{A}\ 1^1B_1$ electronic transition in liquid water [30], the trap sites consisting of favorable local arrangements of several water molecules can be more easily altered [39]. This may affect the $\chi_{trap}(E_{exc})$ curve of Fig. 1(e): The "shoulder" with approximately constant χ_{trap} values for E_{exc} < 8 eV may disappear when the arrangement of water molecules is disturbed by a high CB electron density, and the initiation channel may then partially or completely collapse.

The possible influence of CB electrons on the initiation channel must be taken into account for laser parameters at which seed electrons produced by photoionization are abundant, i.e. for ultrashort pulse durations and for short wavelengths. Furthermore, the simple approach for threshold prediction of IR ns breakdown presented in section 4 cannot be applied in these parameter ranges and all aspects of the breakdown dynamics must be considered. Thus, there is a need for a full model suitable for tracking the breakdown dynamics in a large range of wavelengths and pulse durations [64]. Insights gained in the present study on multiphoton initiation of optical breakdown in water, on the existence of a separate excitation channel for breakdown initiation, and on the wavelength dependence of seed electron density will be important building blocks for such modeling efforts.

ACKNOWLEDGMENT

This work was supported by U.S. Air Force Office of Scientific Research, grant FA 8655-05-1-3010.

---

* Corresponding author: vogel@bmo.uni-luebeck.de

+ thomas.trickl@imk.fkz.de

FIGURE CAPTIONS

Fig. 1. Literature data on ionization pathways in liquid water, and consequences for breakdown initiation. (a) Energy dependence of quantum efficiency QE_{esc} for the creation of long-lived solvated electrons $e^-_{aq(esc)}$ that have escaped geminate recombination [32]. (b) Probability P_{esc} for excess electrons to escape recombination [30]. (c) Average ejection length r_{ej} of the excess electrons [30]. (d) Initial quantum efficiency QE_{ini} of excess electron formation derived from (a) and (b) by $QE_{ini} = QE_{esc}/P_{esc}$. (e) Density of pre-existing trap sites for solvated electron formation derived from (c) and (d) by $\chi_{trap} = QE_{ini}/ (4/3\pi r^3_{ej})$. The energy dependence of P_{esc} and r_{ej} in (b) and (c) suggests that vertical ionization into the CB dominates for $E_{exc} \geq 11$ eV, and autoionization becomes important for $E_{exc} \geq 9.5$ eV. For $E_{exc} < 9.3$ eV, all excess electrons relax into the solvated state or recombine. Nevertheless, breakdown initiation is possible if e^-_{aq} absorb further photons that promote them into the CB, as depicted as "upconversion path" in Figure 2.

Fig. 2. Ionization and geminate recombination pathways in liquid water as suggested by the data in Fig. 1. For large excitation energies, ionization can proceed via vertical ionization ($E_{exc} \geq 11$ eV) or autoionization ($E_{exc} \geq 9.5$ eV), while for $E_{exc} < 9.3$ eV, ionization is possible only as a two-step process involving solvated electron creation followed by upconversion of e^-_{aq} into the conduction band. The latter process competes with geminate recombination.

Fig. 3. Setup for the examination of the wavelength dependence of nanosecond optical breakdown in water by means of a single-longitudinal-mode OPO.

Fig. 4. Pulse shape of a slm OPO pulse of 900 nm wavelength and 2.3 ns duration (a), compared to single-frequency and longitudinal multimode Nd:YAG laser pulses of 1064 nm wavelength and 11.2 ns duration in (b) and (c), respectively. Below each pulse shape, the corresponding breakdown probability curves are shown in (d), (e), and (f). The threshold sharpness is given by $S = E_{th} / \Delta E$, with ΔE being the energy range between 10 % and 90 % breakdown probability.

Fig. 5. Wavelength dependence of duration and M^2 values of laser pulses used in the present study determined for focusing at $NA = 0.9$. The beam quality is optimal around the center wavelength of each of the two optics sets used for the OPO and deteriorates at the borders of each range. Since the M^2 values exhibited little scatter and a clear $M^2(\lambda)$ trend,

measurements were performed for only 12 wavelengths, and intermediate values were interpolated. For the pulse duration, no systematic dependence on λ is observed.

Fig. 6. Wavelength dependence of the threshold for plasma-mediated bubble formation by slm OPO pulses focused at NA = 0.8 and NA = 0.9, and averaged values. The order of the multiphoton process required to cross the band gap in different regions of the $I_{th}(\lambda)$ spectrum is denoted by k. Transitions zones are marked in grey.

Fig. 7. Wavelength dependence of avalanche ionization rate (dashed line) and multiphoton ionization rate (solid line) calculated for E_{gap} = 9.5 eV and E_{ini} = 6.6 eV, respectively. MP-ionization rate is plotted in log scale, while avalanche ionization rate is in linear scale. All calculations assume an irradiance of 3.5×10^{11} W/cm^2, which is the average I_{th} value in the investigated wavelength range.

Fig. 8. Comparison of predictions for $I_{th}(\lambda)$ based on Eq. (2) with the experimentally determined spectrum (average values from both NAs). Calculations were performed for 2 ns pulse duration. (a) Fits for E_{ini} = 6.6 eV assuming either a constant ρ_{seed} value of 3.3×10^{14} cm^{-3} (blue line), or a wavelength-dependent seed electron density that varies according to ρ_{seed} (cm^{-3}) = $10^{A\lambda\,(nm)\,+\,B}$ (green line). (b) Fit assuming a wavelength dependent ρ_{seed} and a linear decrease of E_{ini} from 6.7 eV at the position of the first peak to 6.43 eV at the second peak (red line; fit parameters see text).

Fig. 9. Temporal evolution of the density of electrons entering the CB via photoionization. The solid line depicts $\rho_{ini}(t)$ obtained via the initiation channel through multiphoton excitation into the intermediate energy level, E_{ini} = 6.6 eV, followed by immediate upconversion into the CB. The dashed line represents the electron density produced by MPI across the entire bandgap, E_{gap} = 9.5 eV, which is almost 6 orders of magnitude smaller than ρ_{ini}. Calculation parameters are the same as for Fig. 8(b) at λ = 800 nm: $I_{th} = 3.76 \times 10^{15}$ W/m^2, $\tau_{gem\text{-}rec}$ = 60 ps, $\rho_{seed} = 3.67 \times 10^{15}$ cm^{-3}. The arrow indicates the time at which the critical seed electron density for avalanche ionization (AI) is reached (45 ps after the peak of the 2-ns laser pulse). Afterwards, the free electron density rapidly increases to full ionization [4,64].

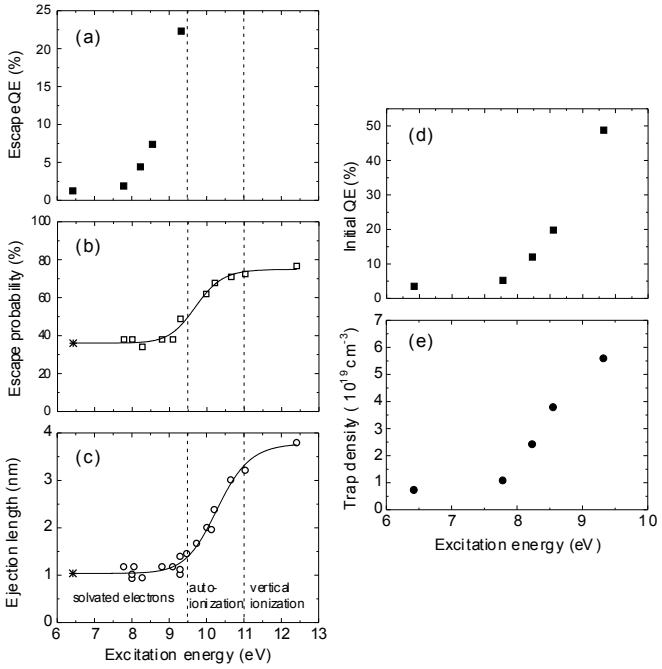
(a)
Escape QE (%)
(b)
Escape probability (%)
(c)
Ejection length (nm)
solvated electrons
auto-ionization
vertical ionization
Excitation energy (eV)
(d)
Initial QE (%)
(e)
Trap density (10^{19} cm^{-3})
Excitation energy (eV)

Figure 1

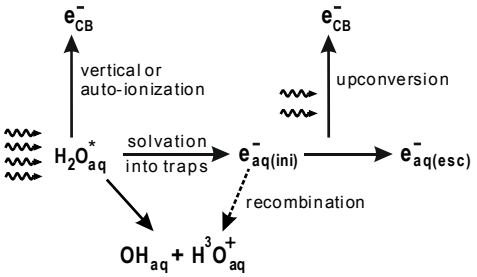
e⁻CB
vertical or
auto-ionization
e⁻CB
upconversion
H2O*aq
solvation
into traps
e⁻aq(ini)
e⁻aq(esc)
recombination
OHaq + H3O+aq

Figure 2

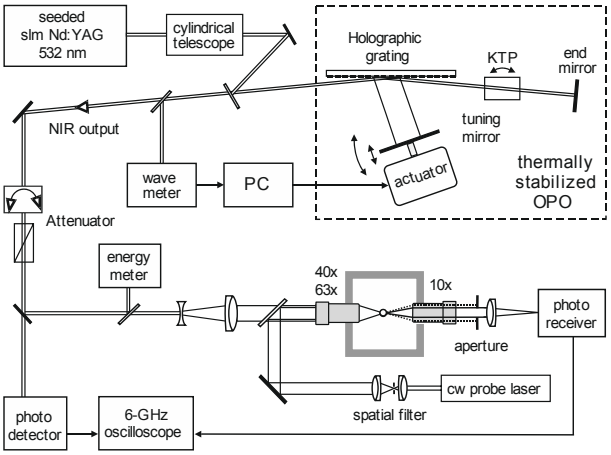
seeded
slm Nd:YAG
532 nm
cylindrical
telescope
Holographic
grating
KTP
end
mirror
NIR output
tuning
mirror
wave
meter
PC
actuator
thermally
stabilized
OPO
Attenuator
energy
meter
40x
63x
10x
photo
receiver
aperture
cw probe laser
spatial filter
photo
detector
6-GHz
oscilloscope

Figure 3

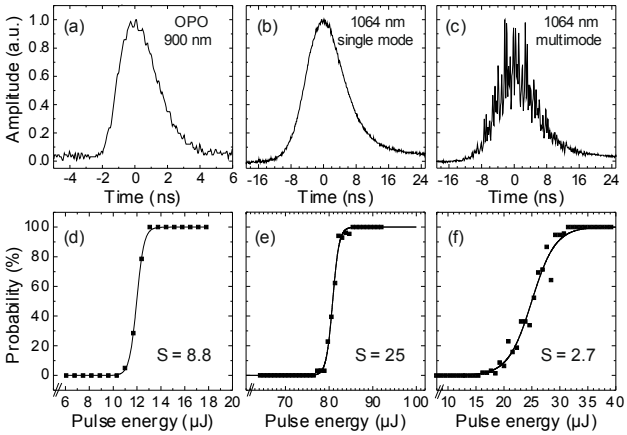
(a)
OPO
900 nm
(b)
1064 nm
single mode
(c)
1064 nm
multimode
Amplitude (a.u.)
Time (ns)
(d)
(e)
(f)
Probability (%)
S = 8.8
S = 25
S = 2.7
Pulse energy (μJ)

Figure 4

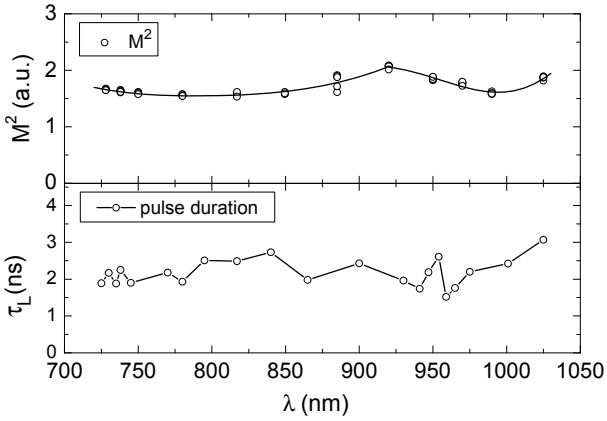
M2
M2 (a.u.)
pulse duration
τL (ns)
λ (nm)
0
1
2
3
4
700
750
800
850
900
950
1000
1050

Figure 5

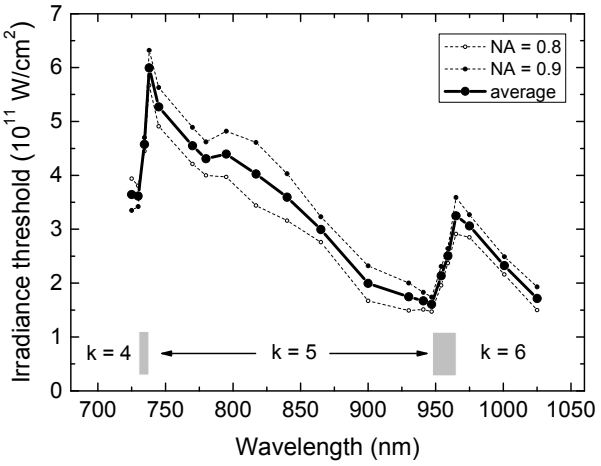
Irradiance threshold (10^{11} W/cm^2)
Wavelength (nm)
NA = 0.8
NA = 0.9
average
k = 4
k = 5
k = 6
0
1
2
3
4
5
6
7
700
750
800
850
900
950
1000
1050

Figure 6

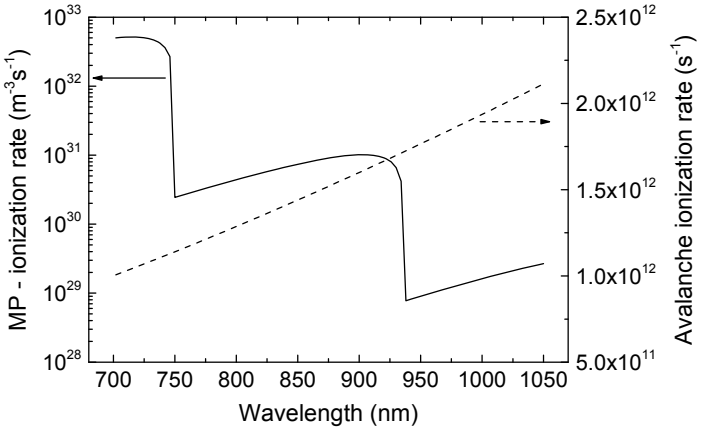
MP - ionization rate (m-3s-1)
Avalanche ionization rate (s-1)
Wavelength (nm)
10^33
10^32
10^31
10^30
10^29
10^28
2.5x10^12
2.0x10^12
1.5x10^12
1.0x10^12
5.0x10^11
700
750
800
850
900
950
1000
1050

Figure 7

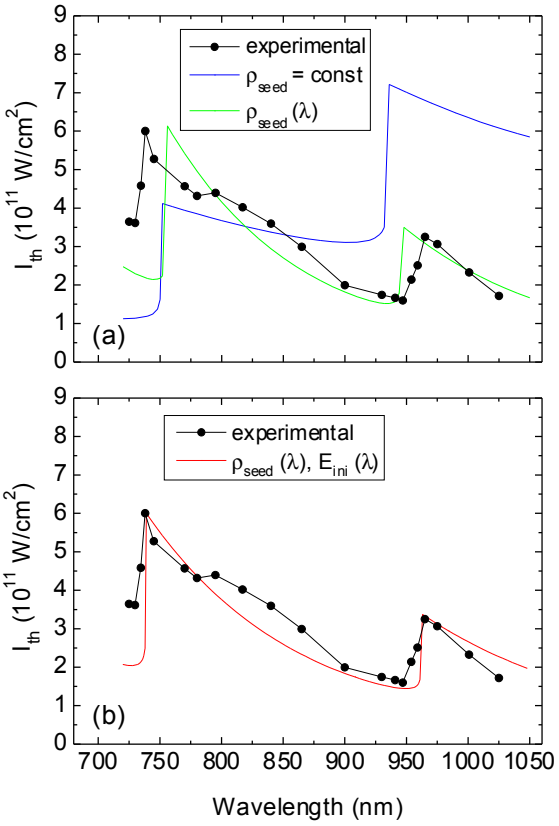
experimental
ρseed = const
ρseed (λ)
(a)
experimental
ρseed (λ), Eini (λ)
(b)
Ith (10^11 W/cm^2)
Wavelength (nm)
0
1
2
3
4
5
6
7
8
9
700
750
800
850
900
950
1000
1050

Figure 8

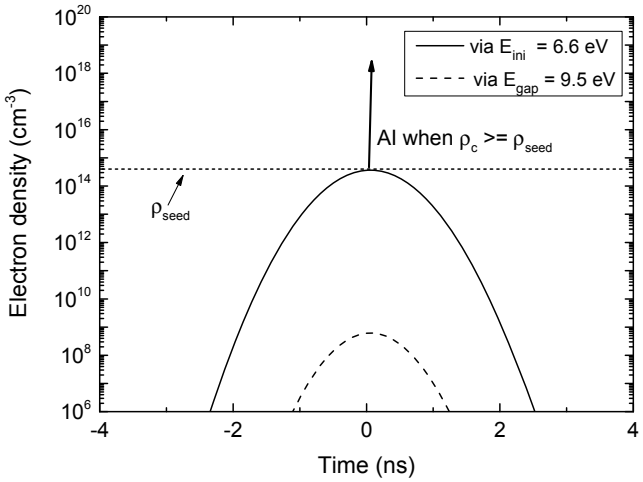
Electron density (cm^{-3})
10^{20}
10^{18}
10^{16}
10^{14}
10^{12}
10^{10}
10^{8}
10^{6}
-4
-2
0
2
4
Time (ns)
via E_{ini} = 6.6 eV
via E_{gap} = 9.5 eV
AI when $\rho_c >= \rho_{seed}$
ρ_{seed}

Figure 9

REFERENCES

1. A. Vogel, P. Schweiger, A. Frieser, M. Asiyo, and R. Birngruber, *Intraocular Nd:YAG laser surgery: damage mechanism, damage range and reduction of collateral effects.*, IEEE J. Quant. Electron. **26**, 2240 (1990).
2. T. Juhasz, F. H. Loesel, R. M. Kurtz, C. Horvath, J. F. Bille, and G. Mourou, *Corneal refractive surgery with femtosecond lasers*, IEEE J. Sel. Top. Quant. **5**, 902 (1999).
3. D. V. Palanker, M. S. Blumenkranz, D. Andersen, M. Wiltberger, G. Marcellino, P. Gooding, D. Angeley, G. Schuele, B. Woodley, and M. Simoneau, *Femtosecond laser-assisted cataract surgery with integrated optical coherence tomography*, Sci. Transl. Med. **2**, 58ra85 (2010).
4. A. Vogel, J. Noack, G. Huettman, and G. Paltauf, *Mechanisms of femtosecond laser nanosurgery of cells and tissues*, Appl. Phys. B. **81**, 1015 (2005).
5. D. J. Stevenson, F. J. Gunn-Moore, P. Campbell, and K. Dholakia, *Single cell optical transfection*, J. R. Soc. Interface **7**, 863 (2010).
6. S. H. Chung and E. Mazur, *Surgical applications of femtosecond lasers*, J. Biophotonics **2**, 557 (2009).
7. W. Lauterborn and T. Kurz, *Physics of bubble oscillations*, Rep. Prog. Phys. **73**, 106501 (2010).
8. M. Bass and H. H. Barrett, *Avalanche breakdown and the probabilistic nature of laser-induced damage*, IEEE J. Quant. Electron. **8**, 338 (1972).
9. A. C. Tien, S. Backus, H. Kapteyn, M. Murnane, and G. Mourou, *Short-pulse laser damage in transparent materials as a function of pulse duration*, Phys. Rev. Lett. **82**, 3883 (1999).
10. E. Van Stryland, M. Soileau, A. Smirl, and W. Williams, *Pulse-width and focal-volume dependence of laser-induced breakdown*, Phys. Rev. B **23**, 2144 (1981).
11. C. A. Sacchi, *Laser-induced electric breakdown in water*, J. Opt. Soc. B **8**, 337 (1991).
12. T. Kovalchuk, G. Toker, V. Bulatov, and I. Schechter, *Laser breakdown in alcohols and water induced by λ=1064nm nanosecond pulses*, Chem. Phys. Lett. **500**, 242 (2010).
13. P. K. Kennedy, *A first-order model for computation of laser-induced breakdown thresholds in ocular and aqueous media: Part I - Theory*, IEEE J. Quant. Electron. **31**, 2241 (1995).
14. J. Noack and A. Vogel, *Laser-induced plasma formation in water at nanosecond to femtosecond time scales: calculation of thresholds, absorption coefficients, and energy density*, IEEE J. Quant. Electron. **35**, 1156 (1999).
15. B. C. Stuart, M. D. Feit, S. Herman, A. M. Rubenchik, B. W. Shore, and M. D. Perry, *Nanosecond-to-femtosecond laser-induced breakdown in dielectrics*, Phys. Rev. B **53**, 1749 (1996).
16. P. Balling and J. Schou, *Femtosecond-laser ablation dynamics of dielectrics: basics and applications for thin films*, Rep. Prog. Phys. **76**(2013).
17. S. S. Mao, F. Quere, S. Guizard, X. Mao, R. E. Russo, G. Petite, and P. Martin, *Dynamics of femtosecond laser interactions with dielectrics*, Appl. Phys. A **79**, 1695 (2004).
18. A. Kaiser, B. Rethfeld, M. Vicanek, and G. Simon, *Microscopic processes in dielectrics under irradiation by subpicosecond laser pulses*, Phys. Rev. B **61**, 11437 (2000).
19. N. Bloembergen, *Laser-induced electric breakdown in solids*, IEEE J. Quant. Electron. **10**, 375 (1974).

20. F. Williams, S. P. Varma, and S. Hillenius, *Liquid water as a lone-pair amorphous semiconductor*, J. Chem. Phys. **64**, 1549 (1976).
21. D. Grand, A. Bernas, and E. Amouyal, *Photoionization of aqueous indole: Conduction band edge and energy gap in liquid water*, Chem. Phys. **44**, 73 (1979).
22. Q. Feng, J. V. Moloney, A. C. Newell, E. M. Wright, K. Cook, P. K. Kennedy, D. X. Hammer, B. A. Rockwell, and C. R. Thompson, *Theory and simulation on the threshold of water breakdown induced by focused ultrashort laser pulses*, IEEE J. Quantum. Elect. **33**, 127 (1997).
23. M. D. Feit, A. M. Komashko, and A. M. Rubenchik, *Ultra-short pulse laser interaction with transparent dielectrics*, Appl. Phys. A **79**, 1657 (2004).
24. A. Dubietis, A. Couairon, E. Kucinskas, G. Tamosauskas, E. Gaizauskas, D. Faccio, and P. Di Trapani, *Measurement and calculation of nonlinear absorption associated with femtosecond filaments in water*, Appl. Phys. B **84**, 439 (2006).
25. J. Jiao and Z. Guo, *Modeling of ultrashort pulsed laser ablation in water and biological tissues in cylindrical coordinates*, Appl. Phys. B. **103**, 195 (2011).
26. C. Sarpe, J. Köhler, T. Winkler, M. Wollenhaupt, and T. Baumert, *Real-time observation of transient electron density in water irradiated with tailored femtosecond laser pulses*, New J. Phys. **14**, 075021 (2012).
27. C. Milian, A. Jarnac, Y. Brelet, V. Jukna, A. Houard, A. Mysyrowicz, and A. Couairon, *Effect of input pulse chirp on nonlinear energy deposition and plasma excitation in water*, J Opt Soc Am B **31**, 2829 (2014).
28. R. Kammel, R. Ackermann, J. Thomas, J. Gotte, S. Skupin, A. Tunnermann, and S. Nolte, *Enhancing precision in fs-laser material processing by simultaneous spatial and temporal focusing*, Light-Sci Appl **3**(2014).
29. S. Minardi, C. Milian, D. Majus, A. Gopal, G. Tamosauskas, A. Couairon, T. Pertsch, and A. Dubietis, *Energy deposition dynamics of femtosecond pulses in water*, Appl. Phys. Lett. **105**(2014).
30. C. G. Elles, A. E. Jailaubekov, R. A. Crowell, and S. E. Bradforth, *Excitation-energy dependence of the mechanism for two-photon ionization of liquid H2O and D2O from 8.3 to 12.4 eV*, J. Chem. Phys. **125**, 044515 (2006).
31. M. U. Sander, M. S. Gudiksen, K. Luther, and J. Troe, *Liquid water ionization: mechanistic implications of the H/D isotope effect in the geminate recombination of hydrated electrons*, Chem. Phys. **258**, 257 (2000).
32. D. M. Bartels and R. A. Crowell, *Photoionization yield vs energy in H2O and D2O*, J. Phys. Chem. A **104**, 3349 (2000).
33. A. Migus, Y. Gauduel, J. L. Martin, and A. Antonetti, *Excess electrons in liquid water - First evidence of a prehydrated state with femtosecond lifetime*, Phys. Rev. Lett. **58**, 1559 (1987).
34. T. Goulet, A. Bernas, C. Ferradini, and J. P. Jaygerin, *On the electronic-structure of liquid water - conduction-band tail revealed by photoionization data*, Chem. Phys. Lett. **170**, 492 (1990).
35. R. A. Crowell and D. M. Bartels, *Multiphoton ionization of liquid water with 3.0-5.0 eV photons*, J. Phys. Chem. **100**, 17940 (1996).
36. J. W. Boyle, J. A. Ghormley, Hochanad.Cj, and J. R. Riley, *Production of hydrated electrons by flash photolysis of liquid water with light in first continuum*, J. Phys. Chem. **73**, 2886 (1969).

37. L. Kevan, *Solvated electron-structure in glassy matrices*, Accounts Chem. Res. **14**, 138 (1981).
38. A. Thaller, R. Laenen, and A. Laubereau, *Femtosecond spectroscopy of the hydrated electron: novel features in the infrared*, Chem. Phys. Lett. **398**, 459 (2004).
39. L. Turi and P. J. Rossky, *Theoretical studies of spectroscopy and dynamics of hydrated electrons*, Chem. Rev. **112**, 5641 (2012).
40. M. S. Pshenichnikov, A. Baltuska, and D. A. Wiersma, *Hydrated-electron population dynamics*, Chem. Phys. Lett. **389**, 171 (2004).
41. R. Lian, D. A. Oulianov, I. A. Shkrob, and R. A. Crowell, *Geminate recombination of electrons generated by above-the-gap (12.4 eV) photoionization of liquid water*, Chem. Phys. Lett. **398**, 102 (2004).
42. C. G. Elles, I. A. Shkrob, R. A. Crowell, and S. E. Bradforth, *Excited state dynamics of liquid water: Insight from the dissociation reaction following two-photon excitation*, J. Chem. Phys. **126**(2007).
43. J. L. Li, Z. G. Nie, Y. Y. Zheng, S. Dong, and Z. H. Loh, *Elementary electron and ion dynamics in ionized liquid water*, J. Phys. Chem. Lett. **4**, 3698 (2013).
44. D. N. Nikogosyan, A. A. Oraevsky, and V. I. Rupasov, *Two-photon ionization and dissociation of liquid water by powerful laser UV radiation*, Chem. Phys. **77**, 131 (1983).
45. C. G. Elles, C. A. Rivera, Y. Zhang, P. A. Pieniazek, and S. E. Bradforth, *Electronic structure of liquid water from polarization-dependent two-photon absorption spectroscopy*, J. Chem. Phys. **130**, 084501 (2009).
46. B. D. Bursulaya, J. Jeon, C. N. Yang, and H. J. Kim, *On the photoabsorption spectroscopy of water*, J. Phys. Chem. A **104**, 45 (2000).
47. H. Lu, F. H. Long, R. M. Bowman, and K. B. Eisenthal, *Femtosecond studies of electron cation geminate recombination in water*, J. Phys. Chem. **93**, 27 (1989).
48. M. U. Sander, K. Luther, and J. Troe, *On the photoionization mechanism of liquid water*, Ber. Bunsen. Phys. Chem. **97**, 953 (1993).
49. J. Savolainen, F. Uhlig, S. Ahmed, P. Hamm, and P. Jungwirth, *Direct observation of the collapse of the delocalized excess electron in water*, Nat. Chem. **6**, 697 (2014).
50. K. R. Siefermann, Y. X. Liu, E. Lugovoy, O. Link, M. Faubel, U. Buck, B. Winter, and B. Abel, *Binding energies, lifetimes and implications of bulk and interface solvated electrons in water*, Nat. Chem. **2**, 274 (2010).
51. B. Winter, R. Weber, W. Widdra, M. Dittmar, M. Faubel, and I. V. Hertel, *Full valence band photoemission from liquid water using EUV synchrotron radiation*, J. Phys. Chem. A **108**, 2625 (2004).
52. K. A. Motakabbir, J. Schnitker, and P. J. Rossky, *A comparison of classical and quantum analyses of electron localization sites in liquid water*, J. Chem. Phys. **97**, 2055 (1992).
53. D. H. Son, P. Kambhampati, T. W. Kee, and P. F. Barbara, *Delocalizing electrons in water with light*, J. Phys. Chem. A **105**, 8269 (2001).
54. M. Assel, R. Laenen, and A. Laubereau, *Femtosecond solvation dynamics of solvated electrons in neat water*, Chem. Phys. Lett. **317**, 13 (2000).
55. C. L. Thomsen, D. Madsen, S. R. Keiding, J. Thogersen, and O. Christiansen, *Two-photon dissociation and ionization of liquid water studied by femtosecond transient absorption spectroscopy*, J. Chem. Phys. **110**, 3453 (1999).

56. L. B. Glebov, O. M. Efimov, G. T. Petrovskiĭ, and P. N. Rogovtsev, *Influence of the mode composition of laser radiation on the optical breakdown of silicate glasses*, Sov. J. Quantum Electron. **14**, 226 (1984).
57. A. V. Smith and B. T. Do, *Bulk and surface laser damage of silica by picosecond and nanosecond pulses at 1064 nm*, Appl. Opt. **47**, 4812 (2008).
58. A. Vogel, N. Linz, S. Freidank, and G. Paltauf, *Femtosecond laser induced nanocavitation in water: implications for optical breakdown threshold and cell surgery*, Phys. Rev. Lett. **100**, 038102 (2008).
59. H. Vogelmann and T. Trickl, *Wide-range sounding of free-tropospheric water vapor with a differential-absorption lidar (DIAL) at a high-altitude station*, Appl. Opt. **47**, 2116 (2008).
60. W. R. Bosenberg and D. R. Guyer, *Single-frequency optical parametric oscillator*, Appl. Phys. Lett. **61**, 387 (1992).
61. G. M. Hale and M. R. Querry, *Optical constants of water in the 200-nm to 200-μm wavelength region*, Appl. Opt. **12**, 555 (1973).
62. L. V. Keldysh, *Ionization in the field of a strong electromagnetic wave*, Soviet Physics JETP **20**, 1307 (1965).
63. N. Bityurin and A. Kuznetsov, *Use of harmonics for femtosecond micromachining in pure dielectrics*, J. Appl. Phys. **93**, 1567 (2003).
64. X.-X. Liang, N. Linz, S. Freidank, and A. Vogel, Institute of Biomedical Optics, University of Luebeck, Peter-Monnik-Weg 4, 23562 Luebeck, Germany, are preparing a manuscript to be called: *Unified model of plasma formation, bubble generation and shock wave emission in water for femtosecond to nanosecond laser pulses.*